RADARNET-SUR FIRST WEATHER RADAR NETWORK IN TROPICAL HIGH MOUNTAINS

Jörg Bendix, Andreas Fries, Jorge Zárate, Katja Trachte, Rütger Rollenbeck, Franz Pucha-Cofrep, Renzo Paladines, Ivan Palacios, Johanna Orellana, Fernando Oñate-Valdivieso, Carlos Naranjo, Leonardo Mendoza, Diego Mejia, Mario Guallpa, Francisco Gordillo, Victor Gonzalez-Jaramillo, Maik Dobbermann, Rolando Célleri, Carlos Carrillo, Augusto Araque, and Sebastian Achilles

A cost-effective X-band weather radar network was installed in the high Andes of southern Ecuador to complement an existing sparse rain gauge network in areas frequently affected by El Niño–Southern Oscillation (ENSO) precipitation hazards.

Ecuador is one of the countries in tropical western South America significantly affected by the El Niño–Southern Oscillation (ENSO) phenomenon (Bendix 2000; Vuille et al. 2000; Bendix et al. 2003; Rossel and Cadier 2009). Precipitation hazards such as flooding and rainfall-driven landslides during El Niño (EN) events regularly result in severe agricultural losses and infrastructure damage, particularly on the coast and the western slopes of the Andes (e.g., Vos et al. 1999). Here, ENSO rainfall extremes clearly exceed the natural variability of precipitation in normal, non-ENSO years (Bendix 2004). Table 1 shows the complex spatiotemporal nature of heavy ENSO rainfall as measured by the

AFFILIATIONS: Bendix, Rollenbeck, Trachte, Achilles, and Dobbermann—Laboratory for Climatology and Remote Sensing, Faculty of Geography, University of Marburg, Marburg, Germany; Fries—Laboratory for Climatology and Remote Sensing, Faculty of Geography, University of Marburg, Marburg, Germany, and Departamento de Geología y Minas e Ingeniería Civil, Hidrología y Climatología Working Group, Universidad Técnica Particular de Loja, Loja, Ecuador; Zárate and Mendoza—Departamento de Planificación y Desarrollo Territorial, Gobierno Provincial de Loja, Loja, Ecuador; Oñate-Valdivieso, Pucha-Cofrep, and Gonzalez-Jaramillo—Departamento de Geología y Minas e Ingeniería Civil, Hidrología y Climatología Working Group, Universidad Técnica Particular de Loja, Loja, Ecuador; Palacios and Guallpa—Departamento de Gestión Ambiental, Empresa de Telecomunicaciones, Agua Potable y Alcantarillado de Cuenca, Cuenca, Ecuador; Naranjo—Instituto Nacional de Meteorología e Hidrología, Quito, Ecuador; Araque and Mejia—Instituto Nacional de Meteorología e Hidrología, Loja, Ecuador; Célleri and Orellana—Departamento de Recursos Hídricos y Ciencias Ambientales, Facultad de Ingeniería, Facultad de Ciencias Químicas, Universidad de Cuenca, Cuenca, Ecuador; Gordillo—Fondo Regional del Agua, Loja, Ecuador; Paladines and Carrillo—Naturalza y Cultura International, Loja, Ecuador

CORRESPONDING AUTHOR: Andreas Fries, andy_fries@gmx.de, aefries@utpl.edu.ec

The abstract for this article can be found in this issue, following the table of contents.

DOI:10.1175/BAMS-D-15-00178.1

In final form 23 October 2016

Table 1. Relative anomalies (Δ%) of rainfall during ENSO (El Niño and La Niña) events (1983–2015) from long-term average (1981–2010, column 5) for the main ENSO period of the year (Jan–May). Data are taken from the operational meteorological stations of the Ecuadorian weather service (INAMHI) with long-term availability (see Fig. 1). Station location: CO = coastal plains (Pacific) and A = Andes mountains. Boldfaced and underlined values indicate anomalies higher than 100%, Boldfaced values anomalies are higher than 50%, and Italic values are negative anomalies.

					El Niño						La Niña				
INAMIHI station	Zone	Radar	Elevation (m MSL)	Rain (mm)	*1983*	*1987*	*1992*	*1993*	*1998*	*2015*	1989	1999	*2008*	2011	*2012*
					Δ%	Δ%	Δ%	Δ%	Δ%	Δ%	Δ%	Δ%	Δ%	Δ%	Δ%
Guayaquil	CO	CAXX	5	1,057	**199**	**90**	39	29	**208**	*−14*	*−13*	*−63*	NA	NA	33
Milagro	CO	CAXX	13	1,313	**109**	**68**	**78**	24	**205**	*−11*	19	*−31*	**58**	*−35*	**57**
Paute	A	CAXX	2,289	364	28	NA	*−29*	30	*−7*	*−60*	17	38	33	49	16
Cañar	A	CAXX	3,038	271	14	5	*−32*	40	18	*−11*	5	**57**			
Gualaceo	A	CAXX	2,449	377	17	21	*−32*	7	15	*−14*	23	**63**	**69**	**55**	38
Santa Rosa	CO	GUAXX	13	283	**65**	NA	NA	NA	NA	**134**	NA	NA	NA	NA	**204**
Celica	A	GUAXX	2,700	965	**139**	***−50***	25	**58**	4	33	**149**	*−20*	**68**	*−25*	**75**
Saraguro	A	All	2,525	457	9	*−20*	*−22*	**79**	**1**	*−10*	**56**	**57**	23	*−16*	*−3*
Loja	A	LOXX	2,160	520	23	*−15*	*−12*	20	*−20*	25	22	46	47	22	15
Cariamanga	A	LOXX	1,960	1,084	47	*−30*	*−37*	38	**80**	21	36	46	**51**	5	1

sparse network of long-term operational meteorological stations in southern Ecuador since the Super El Niño of 1982/83 (Fig. 1). The analysis of rainfall anomalies reveals a general strong positive deviation at the coastal plains in the west of southern Ecuador, while the Andean highlands frequently experience below-average precipitation. Obviously, the positive anomalies at the coast (stations Guayaquil and Milagro) were exceptionally enhanced during the super events in 1983 and 1998 (see also Bendix et al. 2011). However, a high spatial variability of this general tendency is indicated by the fact that the zone of high positive rainfall anomalies is extended eastward into the Andes until the station Celica during EN1983, concomitant with strong westerly wind anomalies (Bendix 1999). This extension toward the eastern parts of southern Ecuador was not observed at the station Celica during EN1998. The station Cariamanga presents the reverse of strong positive rainfall anomalies during EN1998 but not during EN1983, where orographic effects on rainfall seemed to play an important role in establishing a second maximum at the south Ecuadorian Andean mountain slopes (Bendix et al. 2003). In contrast to previous super events, the strong EN in 2015/16 showed slightly negative anomalies at the coastal stations (e.g., station Milagro), while strong anomalies occurred in the southernmost parts of Ecuador (station Santa Rosa). Noteworthy is that moderate past EN events (1987, 1992/93) revealed very different spatial patterns of positive and negative anomalies in rainfall. The data show that the location of heavy rain during an event depends on the complex interplay of several factors. These include local variations in sea surface temperature (SST) anomalies, mainly in the Niño-1+2 region, a pattern of anomalies in the larger-scale atmospheric circulation, and modifications of the land–sea-breeze system with precipitation effects up to 100 km inland (Bendix 2000; Bendix and Bendix 2006).

Compared to EN events, the spatial distribution of heavy rainfall is generally inverted during the La Niña (LN) or Pacific cold phases (Table 1). In southern Ecuador, for instance, LN1999 presented strong negative rainfall anomalies at the coastal plains (stations Guayaquil and Milagro), while the higher eastern parts of the Andes (stations Saraguro, Loja, Cariamanga, Gualaceo, and Cañar) widely experienced heavy rains. Yet again, the station Celica is an outlier for the

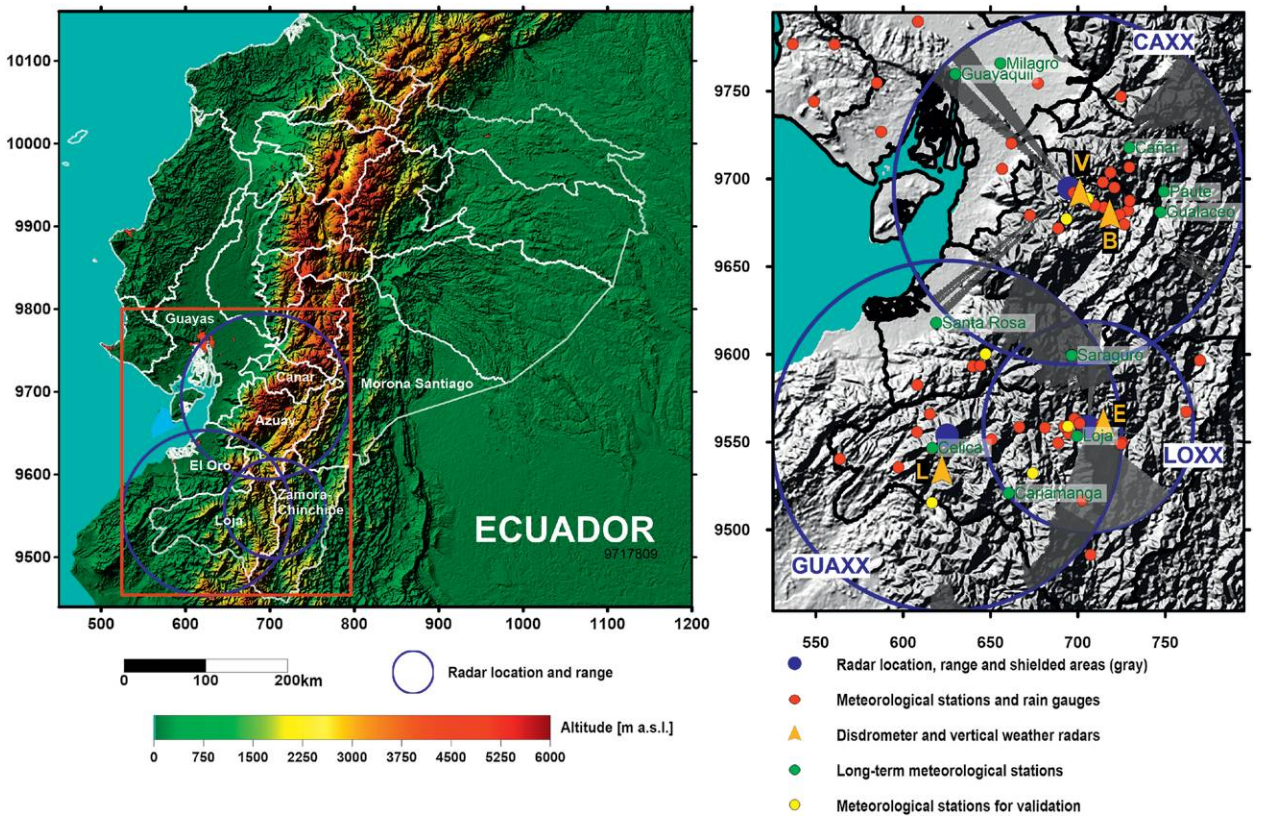

Fig. 1. (left) Coverage and position of RadarNet-Sur. The meteorological stations are operated by INAMHI, the universities of Cuenca (UC) and Loja (UTPL), ETAPA EP, and the German research program PAK823–825. (right) Disdrometer sites are Laipuna (L) for the GUAXX radar, ECSF (E) for the LOXX radar, and La Virgen (V) as well as Balzay (B) for the CAXX radar. Gray hatching denotes areas with complete beam blockage (radar shadows) due to higher terrain. Coordinates UTM 17S are given in kilometers.

lack of consistency in its anomalies. Negative rainfall anomalies occurred during LN1999, while hazardous precipitation was observed during LN1989. The complexity of the situation has grown since the year 2000 because the cold phase of the Pacific decadal oscillation (PDO) has increased the frequency of Modoki events (Bendix et al. 2003). In 2008 and 2012, LN Modokis, a combination of negative and positive SST anomalies in the central Pacific (Niño-3.4 region) and the eastern Pacific (Niño-1+2 region), revealed a specific spatial distribution of rainfall anomalies [for further information on Modoki events, readers may refer to Kao and Yu (2009) as well as to Capotondi et al. (2015)]. Positive rainfall anomalies were observed at the coast (e.g., station Milagro) due to high SSTs in the Niño-1+2 region as well as in different areas of the Andean highlands (stations Paute, Gualaceo, and Celica) triggered by negative SST anomalies in the central Pacific. Thus, LN Modoki events caused different, unexpected changes at individual stations (e.g., station Cariamanga). In summary, a sparse network of rain gauge stations can hardly reveal the complex spatiotemporal dynamics of hazardous rains during ENSO events. Early warning systems urgently need spatial-explicit data to predict resulting flash floods and landslides.

Besides the hazardous rains during ENSO events, water is of utmost importance for irrigation and potable water supply in southern Ecuador, which is mostly fed by the high Andean ecosystems (Páramo). However, changes in land use (Buytaert et al. 2006a, 2007) and climate (Bradley et al. 2006) are threatening the country's water supplies. Approximately half of Ecuador's demand for electricity is met by hydroelectric power generation, making the atmospheric water supply vital to the country (Peláez-Samaniego et al. 2007). Here, the Rio Paute hydroelectric power plant in the south Ecuadorian Andes and its catchment, which is covered by the RadarNet-Sur network, is by far the most important facility in the country (Posso et al. 2015). Therefore, proper spatiotemporal precipitation monitoring is a tangible contribution to these rain-dependent activities in southern Ecuador.

Average precipitation in the Ecuadorian Andes is also characterized by a high spatiotemporal variability

due to the dominant influence of mesoscale processes (see, e.g., Bendix et al. 2009; Trachte et al. 2010). The works of Buytaert et al. (2006b), Xie et al. (2011), and Campozano et al. (2016) reveal that spare rain gauge networks are insufficient at detecting variability in rainfall, especially in mountainous regions. Additional research points out that rain in complex terrain cannot properly be predicted with weather forecast models because they still struggle to provide accurate precipitation estimates, especially where convective precipitation is dominant (Wulfmeyer et al. 2008, 2011; Zollo et al. 2016).

WEATHER RADAR NETWORKS. Weather radar networks deliver high-resolution spatiotemporal information that could offer a viable solution to the problems mentioned above. Despite their indispensable utility for weather forecasting and disaster prevention with regard to spatiotemporal rainfall assessments, radar networks are currently less developed in South America as compared to industrialized countries (Meischner et al. 1997; Serafin and Wilson 2000). The U.S. Next Generation Weather Radar (NEXRAD) network, a prominent example, was recently upgraded to dual-polarization (DP) technology. DP technology

Fig. 2. (top left) X-band scanning instruments of RadarNet-Sur: radar GUAXX RS120 RAINSCANNER on Cerro Guachauro (3,100 m MSL), (top right) GUAXX radar processing unit with backup power supply, (bottom left) radar LOXX LAWR at El Tiro (2,850 m MSL), and (bottom right) radar CAXX RS120 RAINSCANNER on Cerro Paraguillas (4,450 m MSL).

eliminates some problems associated with the previous Doppler systems because it improves the detection of hydrometeor types, nonweather targets, and heavy rains (Hall et al. 1980; Herzegh and Jameson 1992; Brandes et al. 2002). In countries like the United States, highly sophisticated mobile radar systems are even deployed in education (Bell et al. 2015). However, DP technology is hardly affordable for most countries, and economically developing parts of the world are nearly devoid of any operational weather radar network. In their stead, sophisticated space missions currently serve to broaden the coverage of precipitation estimates at a global level (Hou et al. 2014).

The repurposing of single-polarization (SP) X-band marine radar (Jensen 2002; Lengfeld et al. 2014) has recently made it possible to build cost-effective ground radar networks. However, SP X-band systems have a long-standing history of known uncertainty, including (i) calibration, (ii) radar reflectivity (Z)–rain rate (R) relations, (iii) discerning between different types of liquid and solid precipitation particles to derive an adapted Z–R relation, (iv) clutter contamination and beam blockage, and (v) beam attenuation [Wilson and Brandes (1979) and many thereafter]. In addition, mountainous terrain enhances most of these known problems (Delrieu et al. 1999). Therefore, several approaches have been developed, including procedures to minimize the uncertainties by blending the radar signal with rain gauge observations where available (Seo and Breidenbach 2002), which can partially mitigate these problems (e.g., Germann et al. 2006).

This article summarizes our initial experience with the newly implemented RadarNet-Sur in southern Ecuador. The network's SP X-band radars cost approximately $120,000 (U.S dollars), while more sophisticated C-band radars, used by weather services in economically advanced countries, are in the range of millions of dollars (Rollenbeck and Bendix 2006, 2011; Selex 2011). The latter represents an unaffordable radar network solution for most South American countries. RadarNet-Sur is an interdisciplinary effort involving German radar scientists and Ecuadorian stakeholders and serves as a prototype that may be replicable in other mountainous regions of economically developing countries. The network is the result of a knowledge transfer and capacity building project with the goal of bringing weather radar technology into service in southern Ecuador, as a model for a future national network. After a description of the instruments, data, and web infrastructure, our initial work related to data correction and calibration is presented before some examples are given that underpin the potential benefits of the network. The article closes with an outlook for future developments.

INFRASTRUCTURE OF THE RADAR NETWORK. Three scanning SP X-band radars form the basis of the RadarNet-Sur network (Figs. 1, 2; Table 2). The older system, a Local Area Weather Radar (LAWR) purchased from the Danish Hydraulic Institute (DHI), is located at the summit of El Tiro (2,850 m MSL; LOXX radar) east of the city of Loja. The LAWR is based on the marine radar Furuno 1525MK3 and transmits at a frequency of 9,410 ± 30 MHz with a bandwidth of 3 MHz and a pulse length of 1.2 μs at a repetition rate of 600 Hz. The corresponding fan beam antenna has a horizontal beamwidth of 0.92° and a vertical beamwidth of 10° (up and down). Internal resampling of the system returns image sizes of 240 × 240 pixels with a spatial resolution of 500 m at a maximum range of 60 km [for further details refer to Jensen (2002), Rollenbeck and Bendix (2006), and Pedersen et al. (2010)]. Image resolution can be sharpened up to 100 m by reducing the range (Fries et al. 2014).

The two newer systems are RS120 RAINSCANNER instruments (RS120) produced by Selex ES GmbH (Germany). They have a transmission frequency of 9,410 ± 30 MHz, a bandwidth of 2.5 MHz, and a pulse length of 1.2–0.5 μs at a repetition rate of 833–1,500 Hz. These systems have parabolic antennae

Table 2. Scanning X-band (9,410 MHz) radar systems used in RadarNet-Sur.

Radar	Location (° and m MSL)	Type	Manufacturer	Nominal range (km)/resolution (m)
Cajas (CAXX)	2°45′S, 79°16′W; 4,450	RS120 RAINSCANNER	Selex ES	Max 100/500–100
Loja (LOXX)	3°59′S, 79°08′W; 2,850	LAWR	DHI	60/500 30/250 15/100
Guachaurco (GUAXX)	4°02′S, 79°52′W; 3,100	RSI 20 RAINSCANNER	Selex ES	Max 100/500–100

with a horizontal and a vertical beamwidth of 2°. The RS120 have a maximum range of 100 km and provide user-defined images with different ranges and radial resolutions (100 to 500 m). The westernmost RS120 system is located on Cerro Guachaurco (3,100 m MSL; GUAXX radar) near the city of Celica. The highest radar unit of the network (and to our knowledge the highest worldwide) is situated at the edge of the Cajas National Park on Cerro Paraguillas (4,450 m MSL; CAXX radar) near the city of Cuenca, covering the headwaters of the Rio Paute catchment.

Additional instruments for improved rain estimates. To overcome the limitations of operating radar instruments in complex terrain and to improve the quality of the SP X-band weather radar retrievals, several project partners installed networks of ground-based observation stations (Figs. 1–3). The basic network of Automatic Weather Stations (AWS) and rain gauge observations includes the sparse operational network of the Ecuadorian Weather Service [Instituto Nacional de Meteorología e Hidrología (INAMHI)] and involves equipment from other public institutions. This is complemented by universities and research project AWS networks, which deliver rain gauge data in a high temporal resolution (10 min). The latter also cover remote mountain areas (e.g., Fig. 3) that are largely not covered by the INAMHI's operational network due to the difficulty in accessing them. For specific data adjustment purposes, such as deriving the Z–R relations for different climate regimes with diverging rainfall characteristics (i.e., the Tumbesian dry forest, the mountain rain forest, and the Andean Páramo highlands), each radar area received one dedicated disdrometer site (Table 3).

The main sites in the LOXX area are the meteorological stations around the Estación Científica San Francisco (ECSF) research station (3°58′S, 79°4′W; Rollenbeck et al. 2007), where three instruments are installed (see Fig. 1, E). The first is a Biral VPF-730 present weather sensor, a light scatter instrument capable of measuring precipitation and retrieving a particle size matrix from the amplitude of the intensity and duration of the scintillation signal (Ellis et al. 2006). Because of some uncertainties with oblique particle incidence, the station is complemented by a second instrument, an OTT Parsivel (particle size and velocity) laser optical disdrometer, a light beam

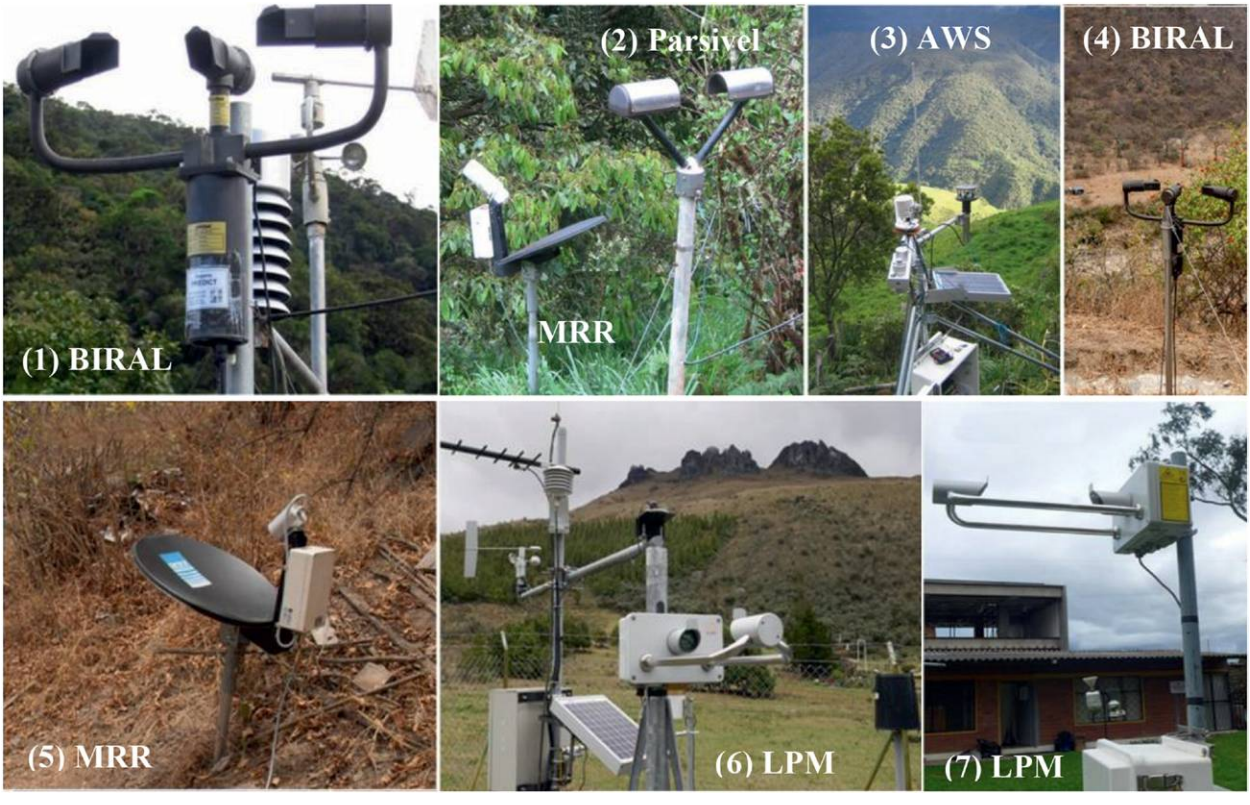

Fig. 3. Instruments at the disdrometer sites: 1) Biral VPF-730, 2) MRR-2 and OTT Parsivel, and 3) Automatic Weather Station (Campbell) in the ECSF area of the mountain rain forest (for LOXX radar). 4) Biral VPF-730 and 5) MRR-2 at the Laipuna field station in the mountain dry forest (for GUAXX radar). 6) LPM and AWS at La Virgen and 7) LPM at Balzay (for CAXX radar).

occlusion-type instrument that utilizes a horizontal light sheet (Löffler-Mang and Joss 2000; Ellis et al. 2006). The third instrument in the array is the vertically pointing frequency-modulated continuous wave (FM-CW) K-band Doppler radar METEK MRR-2 (Klugmann et al. 1996; Bendix et al. 2006).

For the GUAXX radar unit, a Biral VPF-730 and an MRR-2 instrument were installed at the Laipuna research station in the Tumbesian dry forest (see Fig. 1, L). The CAXX radar area is represented by the station La Virgen at 3,626 m MSL in a shrub-dominated (sub-páramo) transition from upland forest to Páramo (Hofstede et al. 2014), where a Thies Clima laser precipitation monitor (LPM; Lanzinger et al. 2006) complements an AWS (see Fig. 1, V). Like the OTT Parsivel, the LPM precipitation monitor is also a light beam occlusion-type instrument that uses a horizontal light sheet to measure drop size distribution (DSD), drop fall velocities, and rainfall (Ellis et al. 2006). A comparison of data recorded by the LPM and Parsivel revealed a strong consistency in the measurements (de Moraes Frasson et al. 2011). A second LPM instrument is situated in the city of Cuenca (station Balzay; see Fig. 1, B) at 2,610 m MSL.

Data transmission and storage. For a radar network to meet stakeholder demands, data must be transmitted in real time, including the publication of radar composite images via a web interface (Cao et al. 2009). Initially, this requires a direct transmission from the remote radar sites (Figs. 1, 2) to the main database, located in the planning department of the provincial government of Loja [Departamento de Planificación y Desarrollo Territorial, Gobierno Provincial de Loja (GPL); Fig. 4]. For the LOXX radar, a general packet radio service (GPRS; cellular phone) connection was introduced, while a normal Internet connection guarantees real-time data transmission from the GUAXX radar. The CAXX radar uses radio transmission via a directional antenna, connecting the radar to the Intranet of Empresa pública municipal de Telecommunicaciones, Agua Potable, Alcantarillado y saneamiento (ETAPA EP) in Cuenca (http://geo.etapa.net.ec/visorradar/), where a gateway redirects the data stream to the GPL database. Every new image is saved in the database configured as a file system with standardized metadata, which is continuously mirrored to a server at the University of Marburg via FTP for backup reasons. The web page (www.radarnetsur.gob.ec) provides information to the public and includes basic information on the radar units, a simple explanation of the measurement principles in English and Spanish, the radar composite loop for all of southern Ecuador, and separate, more detailed maps of the three radar systems in higher spatial resolution for the last 3 h. Currently, the online radar loop displays radar reflectivity corrected for clutter contamination and beam blocking effects.

DATA PROCESSING. Both X-band weather radar systems, the LAWR and the RS120, require customized data processing strategies to combine them in the RadarNet-Sur. Therefore, new procedures were developed to guarantee a reliable rain-rate retrieval for the complex environment of the south Ecuadorian

Table 3. Specific sensors available for calibration.

Radar	Site	Location (° and m MSL)	Instruments	Provided by
CAXX	La Virgen	2°46′S, 79°11′W; 3,626	2x Thies Clima LPM	U Cuenca
	Balzay	2°53′S, 79°02′W; 2,610	2x AWS	
LOXX	ECSF	3°58′S, 79°4′W; 1,860	Biral VPF-730 Metek MRR-2 OTT Parsivel AWS Nubiscope	U Marburg
GUAXX	Laipuna	4°12′S, 79°53′W; 610	Biral VPF-730 Metek MRR-2 AWS	U Marburg U Erlangen

Andes. Because of the restrictions of the LAWR, specific procedures for (i) attenuation, (ii) beam blockage and occultation, as well as (iii) clutter correction had to be programmed and implemented. The RS120 does not have the same kind of technical limitations as the LAWR, but specific routines for image correction and the conversion of calibrated Z to R had to be developed and applied, too, due to the complex terrain where the radars are operating.

The subsequent paragraphs describe the custom-tailored data processing tools for both radar systems, which extend the proprietary software routines of the manufacturers, and the improvements in R retrieval gained by the developments. A detailed description of the algorithm and mathematical background is given in Rollenbeck and Bendix (2011) and Fries et al. (2014).

As supplied by the manufacturer, the LAWR only provides the video signal from the Furuno radar monitor as dimensionless 8-bit counts. The radar reflectivity is not available. Thus, an empirical approach was developed for the conversion from raw counts to radar reflectivity and/or rain rate, which encompasses the following modules.

Geometric attenuation (i) is corrected by applying an exponential function dependent on distance and time because of the wear-out of the magnetron, which reduces the emitter power over time. The correction function amplifies the original signal up to a maximum factor of 64, which is further modified by the cumulated scan line totals to correct two-way attenuation caused by rain fields. (ii) A digital elevation model (DEM) is used to calculate beam blockage and occultation correction after passing obstructions like mountain tops. The returned signals are proportionally scaled up to the remaining beam fraction. Parameters for these procedures are derived from maps of cloud frequency, cloud-top altitude, and long-term average rain distribution (INAMHI 1993; Bendix et al. 2004) to assess a plausible distribution of rain in the LAWR radar range. The routine for clutter removal (iii) is based on radar image time series to determine variance thresholds for affected areas. Pixels with a variance lower than 50% of the

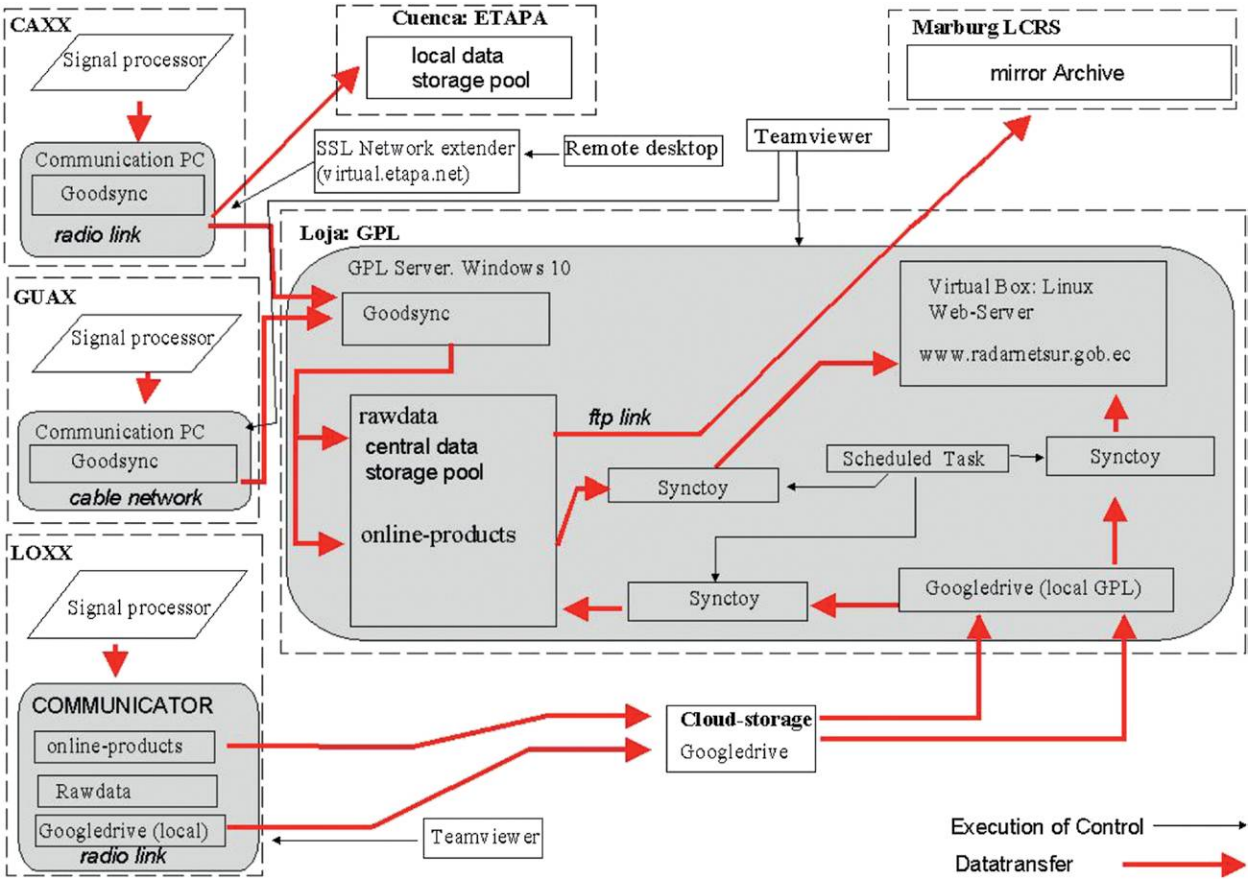

Fig. 4. Data flow diagram of the three radar instruments. Because of the heterogeneous structure, different tools were employed for execution of control (TeamViewer, remote desktop/SSL network extender) and for data synchronization (GoodSync, Google Drive). All connections are password protected.

mean signal are flagged as clutter. Bilinear interpolation techniques fill missing values in the radar map, caused by strong permanent beam obstructions and clutter fields, using data from the next available nonocculted/clutter-free points.

The RS120 instrument provides readings of radar reflectivity. Data processing is executed by a proprietary software application (Selex 2011) whose parameters were adapted to the unique local operation conditions in southern Ecuador. The modified standard procedures are as follows below.

Range and attenuation correction (i) applies a $1r^{-2}$ geometric correction for beam expansion (where r is the distance from the emitter), the squared refraction index of the air (0.93), and a transmit and receive path loss of 0.5 dB. The two-way atmospheric attenuation is set to 0.016 dB km^{-1} and the rain-rate-specific attenuation is approximated by a square function giving an attenuation of 0.15 dB km^{-1} at R = 1 mm h^{-1}, 3.0 dB km^{-1} at R = 10 mm h^{-1}, and 62 dB km^{-1} at R = 100 mm h^{-1}. For the occultation correction (ii) a user-defined log threshold of -3 dBZ is applied to suppress random noise. Furthermore, known occultation sectors are assigned manually, setting the start azimuth angle, stop azimuth angle, and start range. Clutter (iii) is identified by a built-in clutter-decision tree, which additionally requires a deeper analysis of radar images captured under rain-free conditions (Selex 2011). Therefore, user-selected radar images from recent time series are examined to derive the viewing geometry and beam blockage within the radar range. The obtained clutter fields are manually flagged and combined with the clutter fields detected by the built in algorithm. Then, all clutter fields are set to No-Data and submitted to bilinear interpolation. The Selex software allows the operational integration of predefined Z–R relations (iv) based on a gauge-adapted conversion of corrected radar reflectivity to rain rate. However, it was found that the built-in conversion algorithm could not be used because it requires a much higher rain gauge density than available in the study area. Hence, the approach of using continuous relation surfaces (see below) developed for the LAWR was adapted for the RS120 instruments. This empirical approach for quantitative precipitation retrieval (iv) is applied for hourly time steps and establishes a direct relationship between corrected raw counts (LAWR) and Z (RS120) to R.

For each rain gauge location, a daily conversion factor between radar observations (raw counts, respectively, Z) and rainfall is established and then interpolated to form a factor matrix with the resolution of the radar images. The interpolation considers the vertical gradients of rainfall distribution as a drift variable, thus forming anisotropic distance measures between the calibration points. The factor matrix is applied to each hourly radar image to generate the final quantitative precipitation estimate. The images reproduce the spatial distribution of storm cells observed by the radar and the hourly rain rates registered by the rain gauge network. In the future, telemetric rain gauge data will be included to derive R images in near–real time for applications like nowcasting and short-term alert systems, which is a special challenge in southern Ecuador considering its complex terrain.

Because of the strong influence of the topography in this mountainous region on beam propagation, the developed processing chain yields a clear improvement in the agreement between radar data and independent ground observations [shown later in Fig. 9 (bottom)]. Uncorrected data from the radar systems (Fig. 9a) are highly contaminated by beam blockage and clutter. The signal contributions of these disturbances are apparently much higher than the rain signal itself. Eliminating these contaminations from the signal is the crucial step in obtaining stable relations between radar data (raw counts, respectively, Z) and rainfall at the ground station network. Applying the weighted factor matrices, which also account for the local differences in precipitation type and process dynamics of rainfall formation, leads to the strong agreement between calibrated radar rainfall and independent ground rain measurements (Fig. 9b). Rollenbeck and Bendix (2011) presented further evidence for the success of the developed data processing scheme. Their study revealed increasing correlation coefficients by comparing monthly and daily radar rainfall totals with rain gauge data over longer time scales. By applying the customized processing scheme, the determination coefficients increased from 0.12 to 0.34 to 0.8 to 0.98 for monthly and from 0.05 to 0.11 to 0.69 to 0.9 for daily rainfall totals.

Z–R relations. The Z–R relations (the relation of radar reflectivity Z to rain rate R) are generally derived from disdrometer data to improve the rainfall retrieval by adapting to the local rainfall conditions of the radar areas. In the RadarNet-Sur network, Z–R relations can only be applied to the Selex instruments (CAXX and GUAXX). While the analysis of X-band Z–R relations is still ongoing work, we currently use the standard Z–R relation of $Z = 200R^{1.6}$ as set by Selex. However, we have started to derive C-band Z–R relations from the disdrometer data available for each radar site to gain insights into potential variations among the

different rainfall regimes of the network area. For this, the disdrometer data were split into single rainfall events to calculate the A and b parameters of the power law $Z = AR^b$. Then type-specific Z–R relations were calculated for the rainfall categories (e.g., drizzle, rain), which are classified by the present weather-type disdrometer sensors (such as LPM) based on a statistical relationship between particle diameter and fall velocity (Prodi et al. 2011). An example of Z–R relations derived from the two disdrometer sites in the CAXX area is provided in Table 4. The few reported coefficients from the tropics vary between 1.2 and 1.9 for b and 180 and 350 for A (Blanchard 1953; Wood 2005). Our results for both high-altitude sites reveal smaller values, particularly for the drizzle categories at the highest site (La Virgen). This corresponds with Z–R relations of orographic rain reported by Blanchard (1953) in Hawaii and drizzle relations as found by Wood (2005). The result and the very high frequency of light rains in the high Páramo area compared to midelevation sites (Fig. 5) underpin the importance of providing site- and rain type–dependent Z–R relation for radar-based rainfall assessment.

APPLICATION EXAMPLES. The radar network has several applications that benefit the participating stakeholder groups. Water-related applications, that is, the assessment of rainfall input for hydropower

Table 4. C-band Z–R relations for La Virgen and Balzay sites derived from the LPM instruments for 2015 (CAXX radar).

	Site			
	La Virgen (3,626 m MSL)		Balzay (2,610 m MSL)	
Rainfall category	*A*	*b*	*A*	*b*
Light drizzle	2.138	0.472	3.031	0.54
Moderate drizzle	14.343	0.871	16.351	0.908
Light rain	33.128	1.016	45.687	1.032
Moderate rain	43.369	1.139	68.801	1.171
Heavy rain	114.452	1.262	98.385	1.284

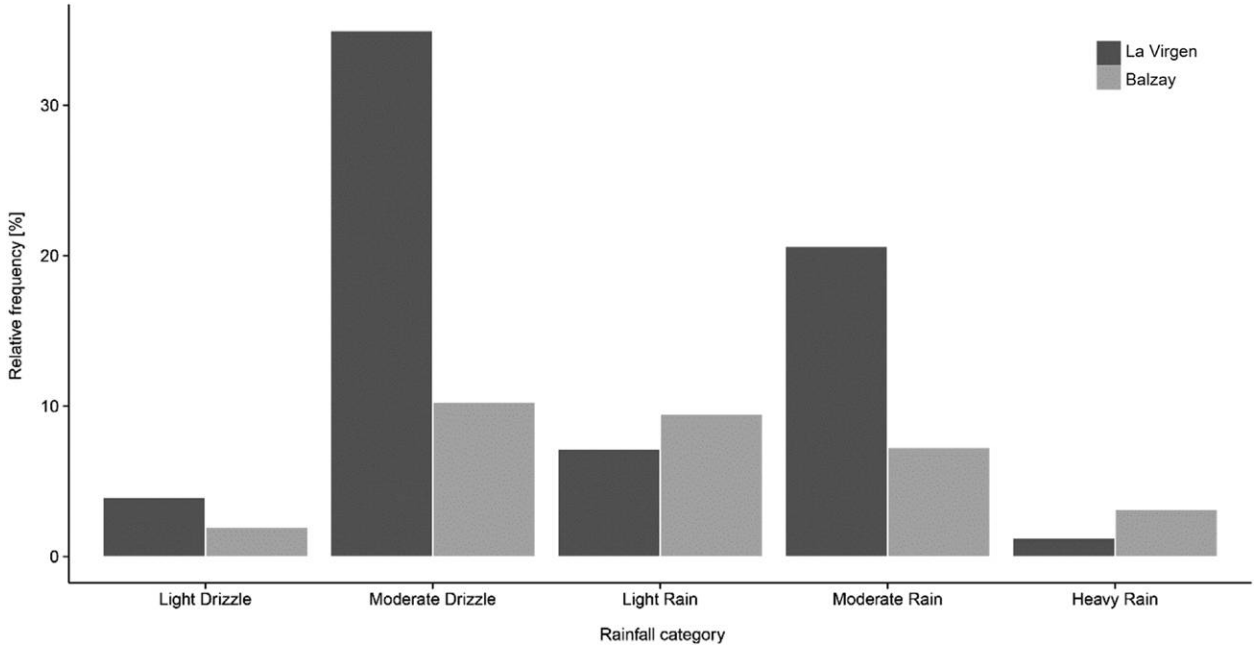

Fig. 5. Occurrence of rain types for very high elevations (La Virgen station) and the midelevation site (Balzay station) in the CAXX radar area observed with LPM data. Drizzle conditions are much more frequent in the high altitude areas of the Cajas National Park where the prevailing easterly airstream meets the unsheltered east-facing slopes of the western cordillera [for the wind situation in easterly exposed crest areas refer to Rollenbeck and Bendix (2011) and Wagemann et al. (2015)].

planning, require spatially explicit information about total rainfall over longer periods. Figure 6 clearly shows that extrapolation techniques based on sparse operational AWS networks are unable to provide reliable data for long-term rainfall assessment. Rainfall totals are particularly underestimated in the high and remote areas of southeastern Ecuador, not covered by AWS stations. Properly validated weather radar estimates help to overcome this problem (see Fig. 6; Rollenbeck and Bendix 2011; Fries et al. 2014).

ENSO (El Niño) rainfall monitoring. Nowcasting heavy rainfall is important for many purposes, such as aviation and disaster prevention. The latter is especially important in southern Ecuador because strong rains are frequently associated with both phases of the

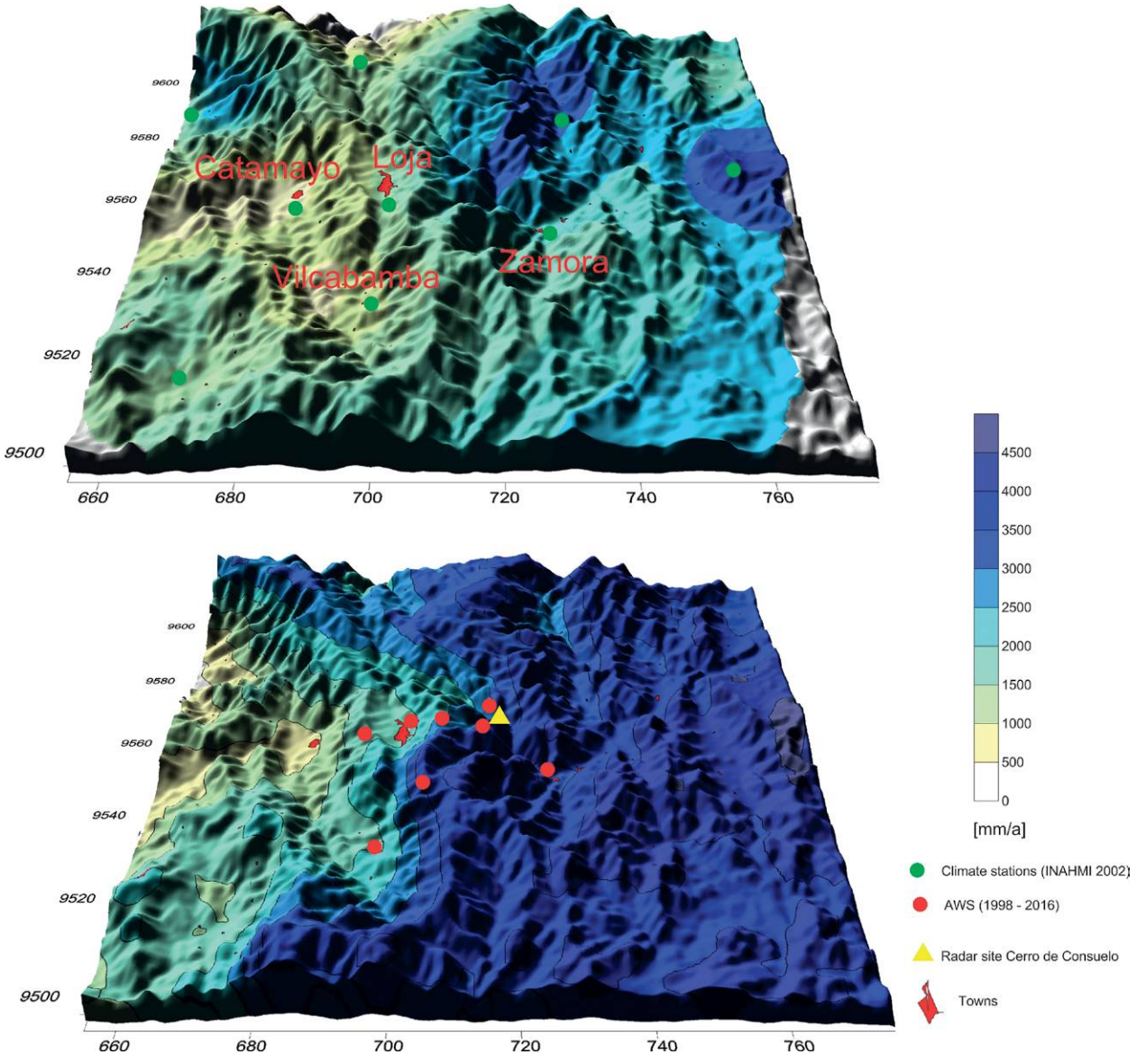

Fig. 6. Comparison of average annual rainfall totals for the ECSF area based on extrapolated rain gauge data (INAMHI) and radar rain retrievals (LOXX radar), superimposed to a DEM. (top) Official map of INAMHI 1964–2000 and (bottom) LAWR radar observations 1998–2009. LAWR data are taken from the LOXX instrument formerly situated on the Cerro del Consuelo close to the ECSF station (4°00′S, 79°03′W; 3,180 m MSL; Rollenbeck and Bendix 2006). Significant extrapolation errors occur in the official rainfall map, such as severe underestimation in large swaths of the higher mountain ranges (e.g., between Vilcabamba and Zamora), which are a very important water supply area. Also, the radar data better represents the orographic enhancement of rainfall on the eastern slopes. Coordinates universal transverse Mercator (UTM) zone 17S (*x* and *y* axis) are given in kilometers.

ENSO phenomenon: EN (mainly coastal Ecuador and western slopes of the western cordillera of the Andes) and LN (eastern cordillera).

According to the Oceanic Niño index (ONI), evaluated by National Oceanic and Atmospheric Administration (NOAA), the most recent 2015/16 EN event presented values of 2.3 [November–January (NDJ) 2015/16], putting it into the same very strong category as the last Super EN in 1997/98. However, for the remainder of the year 2016, SST anomalies returned to near normal values (+0.5 K) in the Niño-1+2 region, and no further extreme rainfall periods were observed in the coastal areas of southern Ecuador. The most significant heavy rainfall event was closely monitored just a few weeks after the full radar network went operational at the end of March 2015, when large positive SST anomalies shifted westward toward the coast of Ecuador. The first impact of this positive anomaly in rainfall was registered during the period 25–31 March 2015. Two major rain peaks were registered: one on the first and the other on the second-to-last day. The period was characterized by statistically significant above-average SST anomalies of up to 6 K (see hatched areas in Fig. 7a). The widespread anomalies were associated with positive deviations in the zonal wind field in the lower troposphere (850-hPa height level; Fig. 7b) that ranged between +2 and +5 m s^{-1} and below normal sea level pressure (SLP) down to −2 hPa (Fig. 7c). The strongest zonal wind field anomalies occurred in the Niño-3 region west of the Galapagos Islands, but westerly wind gusts also reached the coast of Ecuador. The greatest negative deviations of SLP appeared near the coast in the Niño-1+2 region, which corresponded to the anomalous SST pattern. Relative humidity and the wind field in *u*–*w* directions taken at 4°S

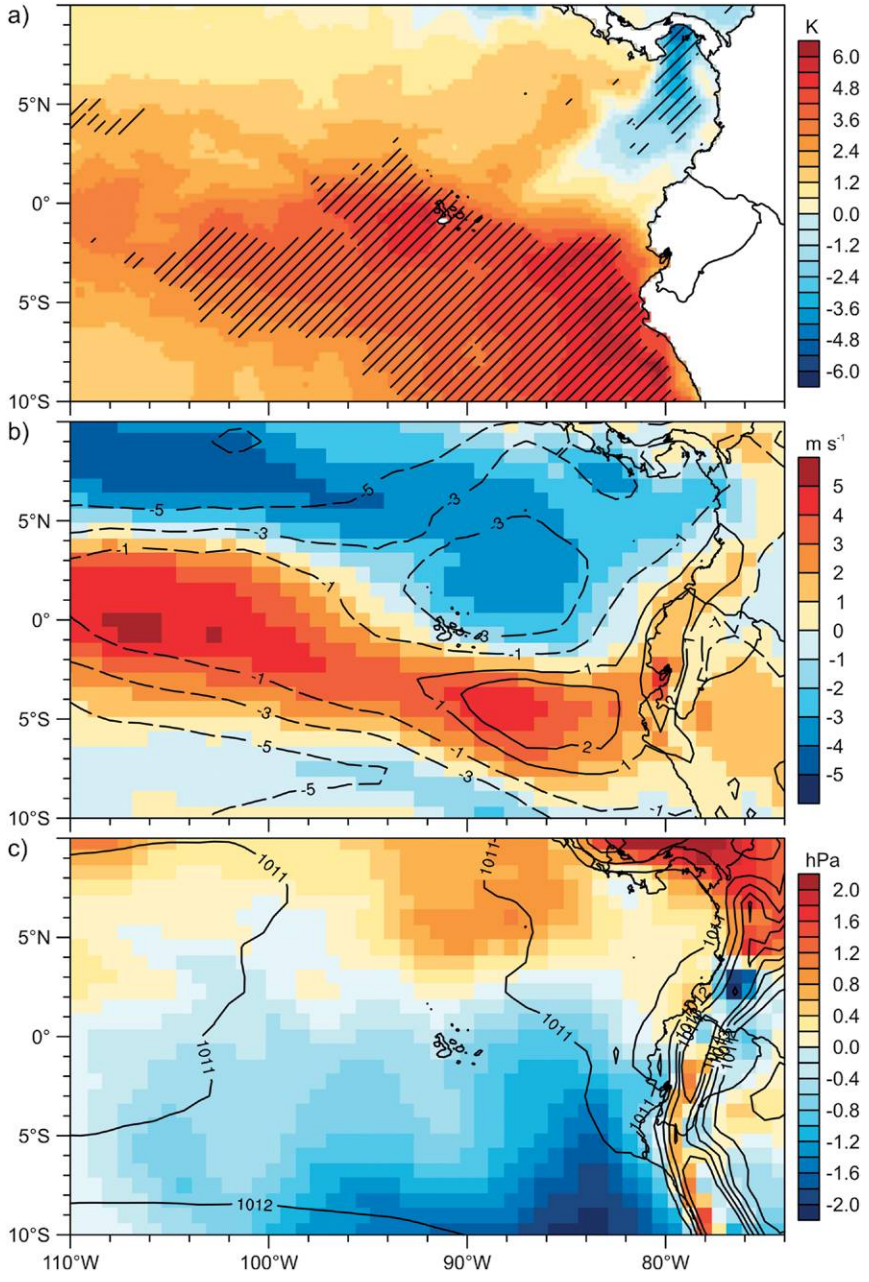

Fig. 7. (a) Anomalous SST (K, shaded) for 25–30 Mar 2015 using the NOAA high-resolution SST data (Reynolds et al. 2007). Hatched areas indicate regions where the SST is above the 95th (and below the 5th) percentile of the 1981–2010 distribution. (b) Mean and anomalous zonal wind field (m s^{-1}), and (c) sea level pressure (hPa) for 25–30 Mar 2015 using the ERA-Interim data (Dee et al. 2011). Shading indicates anomalies relative to the 1981–2010 base period.

elucidate the atmospheric conditions during the two major rain peaks (25 and 30 March; Fig. 8). A westerly component of the airflow was developed in the lower troposphere between 80° and 90°W on both days. The anomalous SST likely induced upward motion in air masses associated with the strongest vertical displacement of moisture near the area of the rain peaks (~80°W).

The radar network and available station data indicate rainfall totals of >400 mm in the southwestern part of the province of Loja (Canton Zapotillo) close to the city of Celica during the final 7 days of March 2015 (Fig. 9). This area (station Sabanilla, 701 m MSL) was hit by heavy rainfall twice, on 25 and 30 March (154 and 201 mm day^{-1} respectively; Fig. 11). Such extremes are exceedingly rare in this dry forest area; in fact, they are near the annual totals normally registered here. March 2015 saw up to 333% of the normal monthly rainfall amounts, 55% of which precipitated during the final 7 days of the month (S. Morocho Quezada, INAMHI Loja, 2016, personal communication). Confirming the European Centre for Medium-Range Weather Forecasts (ECMWF) interim reanalysis (ERA-Interim) data, rainstorm tracking (Fig. 10) applied to the combined radar data from this period confirms several episodes of westerly cell propagation for the entire southwest. This flow carried humidity from the Pacific via northern Peru to the southern Ecuadorian mountain ridges, where orographic effects and local convergence further intensified rainfall formation (Fries et al. 2014). The short period of extreme rainfall claimed the lives of 17 people [official statement Secretaría de Gestión de Riesgos (SGR); international and local press; e.g., BBC Mundo 2015; El Universo 2015], triggered several landslides, and caused considerable damage to agriculture, property, and infrastructure. This extreme rainfall event exemplifies EN's impact on southwestern Ecuador, normally a rather dry region, which is more vulnerable to damage from torrential rain.

Figure 11 shows the daily precipitation amounts and natural hazards (floods and landslides) for the selected period. The orographic enhanced precipitation at the southern part of the coastal cordillera is clearly visible during all days. Particularly in the southern part of the network (radars LOXX and GUAXX), the rainfall regionally exceeded 25 mm day^{-1} (dark blue areas in Fig. 11). Thus, landslides and flooding occurred throughout the entire southern region, especially in the province of Loja and at the upper part of the coastal province of El Oro (see Fig. 1), caused by the predominate wind direction from the southwest. The slopes of the rural highways are

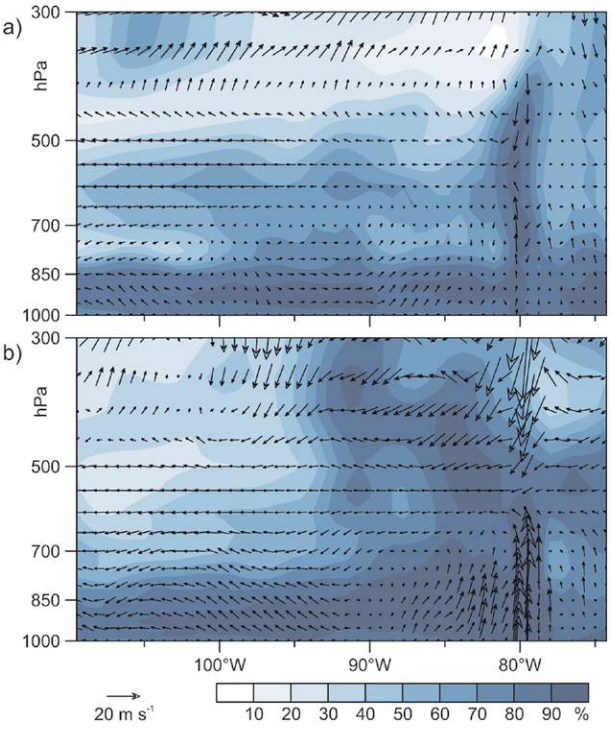

Fig. 8. The *x*–*z* cross section of relative humidity (%, shaded) and wind field in *u*–*w* directions (m s^{-1}, vectors) at 4°S for (a) 25 Mar and (b) 30 Mar 2015 using the ERA-Interim data (Dee et al. 2011).

particularly unstable and prone to landslides during heavy precipitation because of the extreme cuts made for road construction. Frequently, reports of landslides also come from the suburbs of towns and bigger cities because of inadequate land development and construction. Urban flooding is very common, particularly in the city of Loja (Fig. 11, eastern road intersection), because the drainage systems are not designed for such high rainfall amounts. In rural areas, flooding generally occurs at the convergence of larger river systems, whose courses originate in the upper parts of the coastal cordillera. These plane areas are susceptible to inundation of large swaths, which include agricultural land. Most of the reported natural disasters were not triggered by a single rainfall event but rather by the extraordinary precipitation over several days during the study period (M.F. Riofrio Toscano, SGR Zonal 7, 2016, personal communication).

Infrastructure planning. Aside from total rainfall, frequency maps of heavy rainfall are also of great importance for infrastructure surveillance and planning. Rain-driven landslides are a major problem in the Andes of southern Ecuador as they endanger travelers and damage the national road

system (Schuster and Fleming 1986; Solberg et al. 2003; Lozano et al. 2005; Muenchow et al. 2012; Bendix et al. 2013). In addition, the huge amount of sediments in rivers during extreme rainfall periods threatens hydropower generation by depositing the material upstream of the dams (Molina et al. 2008). Vulnerability to rain-driven landslides can be investigated by blending radar data with other relevant data available in geographic information systems (GIS), such as (i) environmental factors, that is, topography, soil, vegetation, or land cover; (ii) risk elements, that is, road network, settlement, and population data; and (iii) additional triggering data, that is, earthquake information, when applicable. To generate landslide susceptibility maps, trigger factors and environmental GIS data are combined in probabilistic models [according to Fell et al. (2008), Remondo et al. (2008), Bendix et al. (2013), and Ochoa-Cueva et al. (2015)].

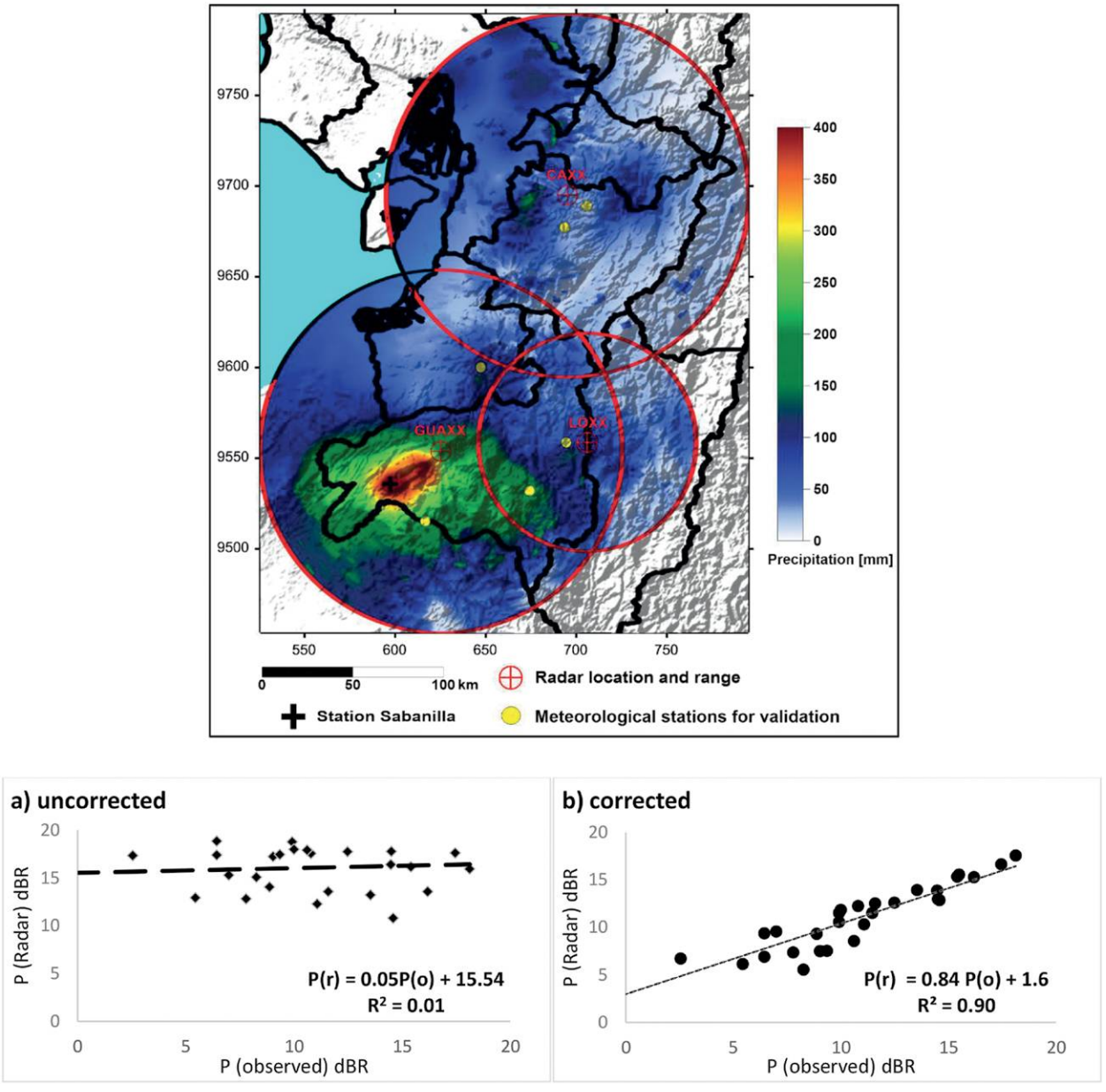

Fig. 9. (top) Rainfall totals for the EN period 25–31 Mar 2015 as seen by RadarNet-Sur (areas of overlap are bilinearly interpolated and the maximum value set at each grid cell; coordinates UTM 17S are given in kilometers). (bottom) Observed daily rainfall (dB*R*) of official INAMHI stations (Ayapamba, Chirimachay, ColT, Gonzanama, Izhcayrrumi cabecera, and Macará; randomly chosen), which were not used for radar rain retrieval, compared to (a) uncorrected daily radar rainfall (dB*R*) and to (b) corrected daily radar rainfall (dB*Z*) presented in a common logarithmic scale.

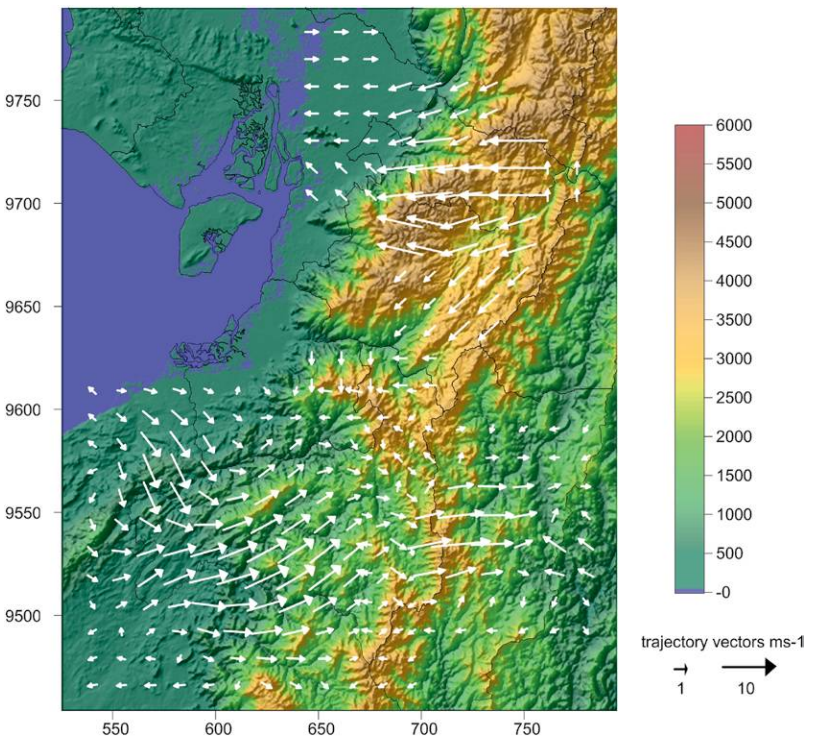

Fig. 10. Average daily motion vectors derived from rain cell tracking for 25 Mar 2015. Westerly flow dominated the southern parts of the province of Loja and Zamora. Convergent structures are also visible close to where the strongest rainfall was registered on that day. Coordinates UTM 17S are given in kilometers.

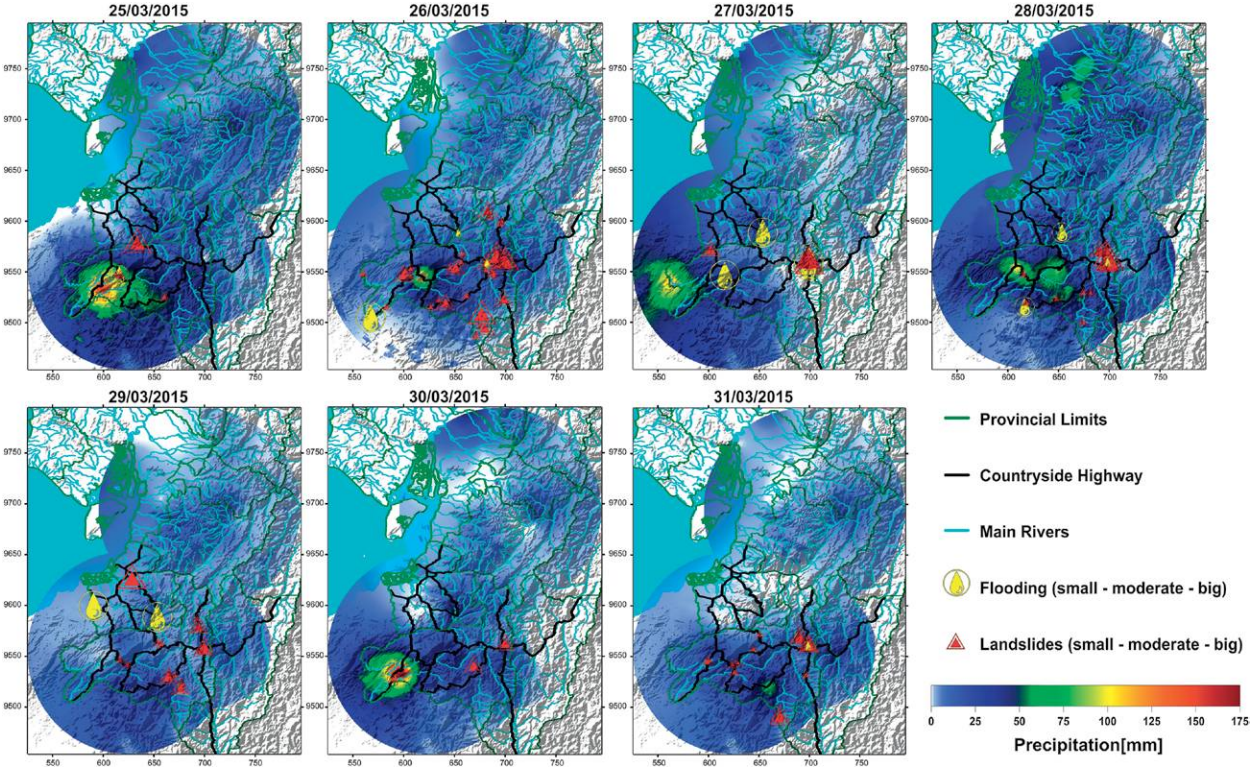

Fig. 11. Daily precipitation maps for the time period 25–31 Mar 2015, including reported landslides and flooding events in southern Ecuador (region 7 = provinces: El Oro, Loja, and Zamora-Chinchipe; data from SGR). Coordinates UTM 17S are given in kilometers. The size of the marks is based on the strength of the event. (Landslides: small = less than 25-m road or less than 5 people affected; moderate = between 25- and 100-m road or between 5 and 10 people affected; and big = more than 100 m of a road or more than 10 people affected. Flooding: small = less than 10 people or less than 5 buildings affected; moderate = between 10 and 50 people or between 5 and 10 buildings affected; and big = more than 50 people or more than 10 buildings affected.)

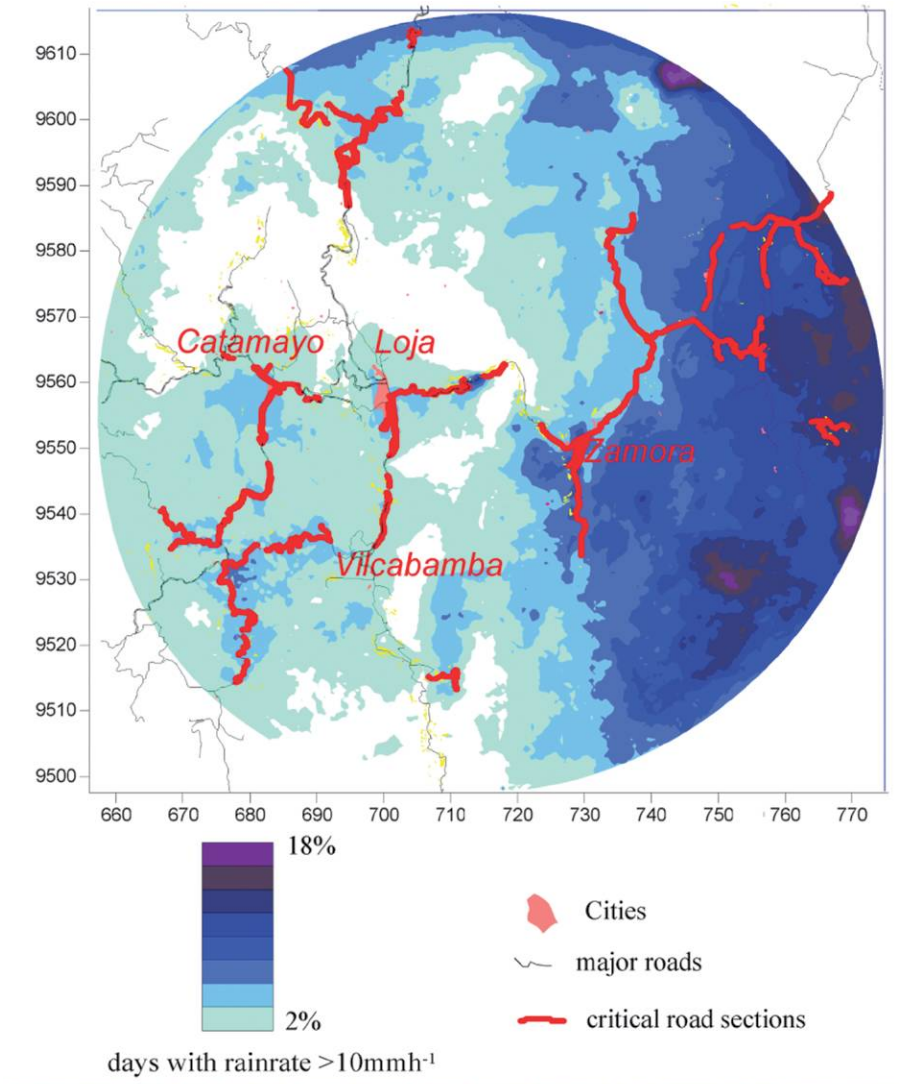

An initial approach to derive a road vulnerability map is based on radar rainfall data and slope angle (Fig. 12). Therefore, a DEM is analyzed to identify slopes with gradients of 30° or greater that are adjacent to major roads (<500 m) in combination with hourly precipitation maps. High risk for rain-driven landslides is indicated if the frequency of days with rain rates above 10 mm h^{-1} exceeds 10 days yr^{-1} in such steep areas (Vorpahl et al. 2012). Figure 12 shows two distinct areas of road vulnerability: east of the city of Loja, road density is lower, but the whole traffic network passing through the steep mountains is threatened by the frequent orographic enhanced advective rainfalls. In

Fig. 12. Risk assessment map for major roads derived from the DEM and radar data (LOXX instrument 1998–2009). As in Fig. 6, the map area is displaced some 10 km east of the current range of the LOXX radar (former location). (top) Areas of high intensity rainfall are shown in shades of blue, representing the frequency of days with rain rates above 10 mm h^{-1}. Coordinates UTM 17S are given in kilometers. (bottom) Landslide caused by heavy rain on the major road Loja-Zamora.

contrast, the main risk factors in the western parts are convective showers of short duration but with high rainfall intensity occurring at certain areas (e.g., west of Vilcabamba).

SUMMARY AND OUTLOOK. The RadarNet-Sur is a great step forward in spatial rainfall assessment and nowcasting in remote and mountainous areas of southern Ecuador. The project's installation phase was extremely successful considering the difficult environment facing Ecuador and its complex topography. It would have been impossible to finalize the network without the contribution of the local stakeholders, in particular, setting up the housing infrastructure, including the construction of a new power line for the CAXX radar and operating the web interface (www.radarnetsur.gob.ec; www.radarnetsur.de). After 1 year of operation, however, it has become clear that maintenance of the radar systems is a major issue; the electronic components are exposed to extreme climate conditions, power spikes, and corrosion. If a system fails, maintenance requires several hours of hiking, which, in the case of the CAXX radar, is above 4,000 m MSL. Thus, maintaining operations will surely be a challenge, especially once the knowledge transfer and capacity building project has been completed. In terms of data processing, the quality of the calibration will be scrutinized in the future. The national weather service (INAMHI) will provide more AWS stations with real-time data transmission and, within the next few years, instantaneous gauge-supported radar image calibration will become possible. A remaining major issue is to derive site-specific X-band Z–R relations for different types of rain. Therefore, a rain-type detection scheme for the radar images will be developed, which allows assignment of the appropriate Z–R to every pixel during a specific rain event, which can be derived from more comprehensive disdrometer data. The web platform will be expanded to provide rain-rate information instead of radar reflectivity and access will be granted to historic data as well. The work on applications, such as the rain cell tracking combined with rainstorm warnings, will also continue. Finally, the consortium endeavors to expand this prototype network into a national system. The project has already received a great level of backing and been endorsed by the most relevant national ministries [Ministerio del Ambiente (MAE), Ministerio de Agricultura, Ganadería, Acuacultura y Pesca (MAGAP), and Secretaría de Gestión de Riesgos (SGR)], which have expressed their willingness to support further developments.

ACKNOWLEDGMENTS. The authors thank the German Research Foundation (DFG) for generously funding the knowledge transfer project RadarNet-Sur (BE1780/31-1 and -2). The gratitude is extended to the DFG-funded programs "Platform for Biodiversity and Ecosystem Monitoring and Research in South Ecuador" (PAK823-825), projects C6 (BE1780/38-1) and C12 (BE1780/37-1, TR1201/1-1), and the previous DFG research units FOR402 and FOR816 for their contribution. The authors very much appreciate the significant financial contributions for infrastructural development and operation made by GPL (Gobierno Provincial de Loja), ETAPA EP (Empresa Pública Municipal de Telecomunicaciones, Agua potable, Alcantarillado y Saneamiento de Cuenca, Ecuador), and the Technical University of Loja (Universidad Técnica Particular de Loja; UTPL). Thanks are also due to the University of Marburg (LCRS) for significantly supporting the purchase of one radar unit and the Dirección General de Aviación Civil del Ecuador (DGAC) and the Ecuadorian telecommunications regulatory authority (Agencia de Regulación y Control de las Telecomunicaciones, SENATEL) for the permission to operate RadarNet-Sur. Finally, we thank Gregory Gedeon for text revision.

REFERENCES

BBC Mundo, 2015: Ecuador: Al menos 17 muertos por temporada de lluvias. BBC Mundo, accessed 22 March 2016. [Available online at www.bbc.com/mundo/ultimas_noticias/2015/03/150331_ultnot_ecuador_muertos_temporada_lluvias_lv.]

Bell, M. M., and Coauthors, 2015: The Hawaiian Educational Radar Opportunity (HERO). *Bull. Amer. Meteor. Soc.*, **96**, 2167–2181, doi:10.1175/BAMS-D-14-00126.1.

Bendix, A., and J. Bendix, 2006: Heavy rainfall episodes in Ecuador during El Nino events and associated regional atmospheric circulation and SST patterns. *Adv. Geosci.*, **6**, 43–49, doi:10.5194/adgeo-6-43-2006.

Bendix, J., 1999: A comparative analysis of the major El Niño events in Ecuador and northern Peru over the last two decades. *Zbl. Geol. Paläntol.*, **7/8**, 1119–1131.

——, 2000: Precipitation dynamics in Ecuador and northern Peru during the 1991/92 El Niño: A remote sensing perspective. *Int. J. Remote Sens.*, **21**, 533–548, doi:10.1080/014311600210731.

——, 2004: Extreme events and climate variability in the Andes of Ecuador and Peru (in German). *Geogr. Rundsch.*, **56**, 10–16.

——, S. Gämmerler, C. Reudenbach, and A. Bendix, 2003: A case study on rainfall dynamics during El Niño/La Niña 1997/99 in Ecuador and surrounding

areas as inferred from GOES-8 and TRMM-PR observations. *Erdkunde*, **57**, 81–93, doi:10.3112/erdkunde.2003.02.01.

——, R. Rollenbeck, and W. E. Palacios, 2004: Cloud detection in the tropics—A suitable tool for climate-ecological studies in the high mountains of Ecuador. *Int. J. Remote Sens.*, **25**, 4521–4540, doi:10.1080/01431160410001709967.

——, ——, and C. Reudenbach, 2006: Diurnal patterns of rainfall in a tropical Andean valley of southern Ecuador as seen by a vertically pointing K-band Doppler radar. *Int. J. Climatol.*, **26**, 829–846, doi:10.1002/joc.1267.

——, K. Trachte, J. Cermak, R. Rollenbeck, and T. Nauß, 2009: Formation of convective clouds at the foothills of the tropical eastern Andes (south Ecuador). *J. Appl. Meteor. Climatol.*, **48**, 1682–1695, doi:10.1175/2009JAMC2078.1.

——, ——, E. Palacios, R. Rollenbeck, D. Göttlicher, T. Nauss, and A. Bendix, 2011: El Niño meets La Niña—Anomalous rainfall patterns in the "traditional" El Niño region of southern Ecuador. *Erdkunde*, **65**, 151–167, doi:10.3112/erdkunde.2011.02.04.

——, and Coauthors, 2013: Natural landslides which impact current regulating services: Environmental preconditions and modeling. *Ecosystem Services, Biodiversity and Environmental Change in a Tropical Mountain Ecosystem of South Ecuador*, J. Bendix et al., Eds., Ecological Studies Series, Vol. 221, Springer-Verlag, 153–170, doi:10.1007/978-3-642-38137-9_12.

Blanchard, D. C., 1953: Raindrop size-distribution in Hawaiian rains. *J. Meteor.*, **10**, 457–473, doi:10.1175/1520-0469(1953)010<0457:RSDIHR>2.0.CO;2.

Bradley, R. S., M. Vuille, H. F. Diaz, and W. Vergara, 2006: Threats to water supplies in the tropical Andes. *Science*, **312**, 1755–1756, doi:10.1126/science.1128087.

Brandes, E. A., G. Zhang, and J. Vivekanandan, 2002: Experiments in rainfall estimation with a polarimetric radar in a subtropical environment. *J. Appl. Meteor.*, **41**, 674–685, doi:10.1175/1520-0450(2002)041<0674:EIREWA>2.0.CO;2.

Buytaert, W., R. Célleri, B. De Bièvre, F. Cisneros, G. Wyseure, J. Deckers, and R. Hofstede, 2006a: Human impact on the hydrology of the Andean páramos. *Earth Sci. Rev.*, **79**, 53–72, doi:10.1016/j.earscirev.2006.06.002.

——, ——, P. Willems, B. De Bievre, and G. Wyseure, 2006b: Spatial and temporal rainfall variability in mountainous areas: A case study from the south Ecuadorian Andes. *J. Hydrol.*, **329**, 413–421, doi:10.1016/j.jhydrol.2006.02.031.

——, V. Iniguez, and B. De Bievre, 2007: The effects of afforestation and cultivation on water yield in the Andean páramo. *For. Ecol. Manage.*, **251**, 22–30, doi:10.1016/j.foreco.2007.06.035.

Campozano, L., R. Célleri, K. Trachte, J. Bendix, and E. Samaniego, 2016: Rainfall and cloud dynamics in the Andes: A southern Ecuador case study. *Adv. Meteor.*, **2016**, 3192765, doi:10.1155/2016/3192765.

Cao, Y., C. Yang, and D. W. Wong, 2009: An interoperable spatiotemporal weather radar data dissemination system. *Int. J. Remote Sens.*, **30**, 1313–1326, doi:10.1080/01431160802508993.

Capotondi, A., and Coauthors, 2015: Understanding ENSO diversity. *Bull. Amer. Meteor. Soc.*, **96**, 921–938, doi:10.1175/BAMS-D-13-00117.1.

Dee, D., and Coauthors, 2011: The ERA-Interim reanalysis: Configuration and performance of the data assimilation system. *Quart. J. Roy. Meteor. Soc.*, **137**, 553–597, doi:10.1002/qj.828.

Delrieu, G., S. Serrar, E. Guardo, and J. D. Creutin, 1999: Rain measurement in hilly terrain with X-band weather radar systems: Accuracy of path-integrated attenuation estimates derived from mountain returns. *J. Atmos. Oceanic Technol.*, **16**, 405–416, doi:10.1175/1520-0426(1999)016<0405:RMIHTW>2.0.CO;2.

de Moraes Frasson, R. P., L. K. da Cunha, and W. F. Krajewski, 2011: Assessment of the Thies optical disdrometer performance. *Atmos. Res.*, **101**, 237–255, doi:10.1016/j.atmosres.2011.02.014.

Ellis, R. A., A. P. Sandford, G. E. Jones, J. Richards, J. Petzing, and J. M. Coupland, 2006: New laser technology to determine present weather parameters. *Meas. Sci. Technol.*, **17**, 1715–1722, doi:10.1088/0957-0233/17/7/009.

El Universo, 2015: Deslizamientos y lluvias afectan provincia de Loja. El Universo, accessed 22 March 2016. [Available online at www.eluniverso.com/noticias/2015/03/25/nota/4702261/deslizamientos-lluvias-afectan-provincia-loja.]

Fell, R., J. Corominas, C. Bonnard, L. Cascini, E. Leroi, and W. Z. Savage, 2008: Guidelines for landslide susceptibility, hazard and risk zoning for land use planning. *Eng. Geol.*, **102**, 85–98, doi:10.1016/j.enggeo.2008.03.022.

Fries, A., R. Rollenbeck, F. Bayer, V. Gonzalez, F. Oñate-Valdivieso, T. Peters, and J. Bendix, 2014: Catchment precipitation processes in the San Francisco valley in southern Ecuador: Combined approach using high-resolution radar images and in situ observations. *Meteor. Atmos. Phys.*, **126**, 13–29, doi:10.1007/s00703-014-0335-3.

Germann, U., G. Galli, M. Boscacci, and M. Bolliger, 2006: Radar precipitation measurement in a

mountainous region. *Quart. J. Roy. Meteor. Soc.*, **132**, 1669–1692, doi:10.1256/qj.05.190.

Hall, M. P. M., S. M. Cherry, J. W. F. Goddard, and G. R. Kennedy, 1980: Rain drop sizes and rainfall rate measured by dual-polarization radar. *Nature*, **285**, 195–198, doi:10.1038/285195a0.

Herzegh, P. H., and A. R. Jameson, 1992: Observing precipitation through dual-polarization radar measurements. *Bull. Amer. Meteor. Soc.*, **73**, 1365–1374, doi:10.1175/1520-0477(1992)073<1365:OPTDPR>2.0.CO;2.

Hofstede, R. G. M., K. J. M. Dickinson, A. F. Mark, and E. Narváez, 2014: Broad transition from cloud forest to Páramo characterizes an undisturbed treeline in Parque Nacional Llanganates, Ecuador. *Arct. Antarct. Alp. Res.*, **46**, 975–986, doi:10.1657/1938-4246-46.4.975.

Hou, A. Y., and Coauthors, 2014: The Global Precipitation Measurement Mission. *Bull. Amer. Meteor. Soc.*, **95**, 701–722, doi:10.1175/BAMS-D-13-00164.1.

INAMHI, 1993: Anuario Meteorológico No. 33, Edicíon Especial, Quito-Ecuador 1995. [Available online at www.serviciometeorologico.gob.ec/wp-content/uploads/anuarios/meteorologicos/.]

Jensen, N. E., 2002: X-band local area weather radar–preliminary calibration results. *Water Sci. Technol.*, **45**, 135–138. [Available online at http://wst.iwaponline.com/content/45/2/135.]

Kao, H. Y., and J. Y. Yu, 2009: Contrasting eastern-Pacific and central-Pacific types of ENSO. *J. Climate*, **22**, 615–632, doi:10.1175/2008JCLI2309.1.

Klugmann, D., K. Heinsohn, and H.-J. Kirtzel, 1996: A low cost 24 GHz FM–CW Doppler radar rain profiler. *Contrib. Atmos. Phys.*, **69**, 247–253.

Lanzinger, E., M. Theel, and H. Windolph, 2006: Rainfall amount and intensity measured by the Thies laser precipitation monitor. *TECO-2006 WMO Technical Conf. on Meteorological and Environmental Instruments and Methods of Observation*, IOM 94, Geneva, Switzerland, WMO, 9 pp. [Available online at https://www.wmo.int/pages/prog/www/IMOP/publications/IOM-94-TECO2006/3%283%29_Lanzinger_Germany.pdf.]

Lengfeld, K., M. Clemens, H. Münster, and F. Ament, 2014: Performance of high-resolution X-band weather radar networks—The PATTERN example. *Atmos. Meas. Tech.*, **7**, 4151–4166, doi:10.5194/amt-7-4151-2014.

Löffler-Mang, M., and J. Joss, 2000: An optical disdrometer for measuring size and velocity of hydrometeors. *J. Atmos. Oceanic Technol.*, **17**, 130–139, doi:10.1175/1520-0426(2000)017<0130:AODFMS>2.0.CO;2.

Lozano, P., R. W. Bussmann, and M. Küppers, 2005: Landslides as ecosystem disturbance—Their implications and importance in South Ecuador. *Lyonia*, **8**, 67–72. [Available online at www.lyonia.org/downloadPDF.php?pdfID=2.386.1.]

Meischner, P., C. Collier, A. Illingworth, J. Joss, and W. Randeu, 1997: Advanced weather radar systems in Europe: The COST 75 action. *Bull. Amer. Meteor. Soc.*, **78**, 1411–1430, doi:10.1175/1520-0477(1997)078<1411:AWRSIE>2.0.CO;2.

Molina, A., G. Govers, J. Poesen, H. Van Hemelryck, B. De Bièvre, and V. Vanacker, 2008: Environmental factors controlling spatial variation in sediment yield in a central Andean mountain area. *Geomorphology*, **98**, 176–186, doi:10.1016/j.geomorph.2006.12.025.

Muenchow, J., A. Brenning, and M. Richter, 2012: Geomorphic process rates of landslides along a humidity gradient in the tropical Andes. *Geomorphology*, **139–140**, 271–284, doi:10.1016/j.geomorph.2011.10.029.

Ochoa-Cueva, P., A. Fries, P. Montesinos, J. A. Rodríguez-Díaz, and J. Boll, 2015: Spatial estimation of soil erosion risk by land-cover change in the Andes of southern Ecuador. *Land Degrad. Dev.*, **26**, 565–573, doi:10.1002/ldr.2219.

Pedersen, L., N. E. Jensen, and H. Madsen, 2010: Calibration of local area weather radar—Identifying significant factors affecting the calibration. *Atmos. Res.*, **97**, 129–143, doi:10.1016/j.atmosres.2010.03.016.

Peláez-Samaniego, M. R., M. Garcia-Perez, L. A. B. Cortez, J. Oscullo, and G. Olmedo, 2007: Energy sector in Ecuador: Current status. *Energy Policy*, **35**, 4177–4189, doi:10.1016/j.enpol.2007.02.025.

Posso, F., J. L. Espinoza, J. Sánchez, and J. Zalamea, 2015: Hydrogen from hydropower in Ecuador: Use and impacts in the transport sector. *Int. J. Hydrogen Energy*, **40**, 15 432–15 447, doi:10.1016/j.ijhydene.2015.08.109.

Prodi, F., C. Caracciolo, L. P. D'Adderio, M. Gnuffi, and E. Lanzinger, 2011: Comparative investigation of Pludix disdrometer capability as present weather sensor (PWS) during the Wasserkuppe campaign. *Atmos. Res.*, **99**, 162–173, doi:10.1016/j.atmosres.2010.09.016.

Remondo, J., J. Bonachea, and A. Cendrero, 2008: Quantitative landslide risk assessment and mapping on the basis of recent occurrences. *Geomorphology*, **94**, 496–507, doi:10.1016/j.geomorph.2006.10.041.

Reynolds, R. W., T. M. Smith, C. Liu, D. B. Chelton, K. S. Casey, and M. G. Schlax, 2007: Daily high-resolution-blended analyses for sea surface temperature. *J. Climate*, **20**, 5473–5496, doi:10.1175/2007JCLI1824.1.

Rollenbeck, R., and J. Bendix, 2006: Experimental calibration of a cost-effective X-band weather radar for climate ecological studies in southern Ecuador.

Atmos. Res., **79**, 296–316, doi:10.1016/j.atmosres.2005.06.005.

——, and ——, 2011: Rainfall distribution in the Andes of southern Ecuador derived from blending weather radar data and meteorological field observations. *Atmos. Res.*, **99**, 277–289, doi:10.1016/j.atmosres.2010.10.018.

——, ——, P. Fabian, J. Boy, W. Wilcke, H. Dalitz, M. Oesker, and P. Emck, 2007: Comparison of different techniques for the measurement of precipitation in tropical montane rain forest regions. *J. Atmos. Oceanic Technol.*, **24**, 156–168, doi:10.1175/JTECH1970.1.

Rossel, F., and E. Cadier, 2009: El Niño and prediction of anomalous monthly rainfalls in Ecuador. *Hydrol. Processes*, **23**, 3253–3260, doi:10.1002/hyp.7401.

Schuster, R. L., and R. W. Fleming, 1986: Economic losses and fatalities due to landslides. *Environ. Eng. Geosci.*, **23**, 11–28, doi:10.2113/gseegeosci.xxiii.1.11.

Selex, 2011: Instruction manual—RainView Analyzer user guide—Release 5.33.0. Selex Systems Integration GmbH Neuss-Rosellen, 84 pp.

Seo, D. J., and J. P. Breidenbach, 2002: Real-time correction of spatially nonuniform bias in radar rainfall data using rain gauge measurements. *J. Hydrometeor.*, **3**, 93–111, doi:10.1175/1525-7541(2002)003<0093:RTCOSN>2.0.CO;2.

Serafin, R. J., and J. W. Wilson, 2000: Operational weather radar in the United States: Progress and opportunity. *Bull. Amer. Meteor. Soc.*, **81**, 501–518, doi:10.1175/1520-0477(2000)081<0501:OWRITU>2.3.CO;2.

Solberg, S., D. Hale, and J. Benavides, 2003: Natural disaster management and the road network in Ecuador: Policy issues and recommendations. Inter-American Development Bank Rep. IDB 39838, 20 pp.

Trachte, K., R. Rollenbeck, and J. Bendix, 2010: Nocturnal convective cloud formation under clear-sky conditions at the eastern Andes of south Ecuador. *J. Geophys. Res.*, **115**, D24203, doi:10.1029/2010JD014146.

Vorpahl, P., H. Elsenbeer, M. Märker, and B. Schröder, 2012: How can statistical models help to determine driving factors of landslides? *Ecol. Modell.*, **239**, 27–39, doi:10.1016/j.ecolmodel.2011.12.007.

Vos, R., M. Velasco, and E. Labastida, 1999: Economic and social effects of "El Niño" in Ecuador, 1997-8. ISS Working Paper Series/General Series 292, 55 pp. [Available online at http://repub.eur.nl/pub/19037/.]

Vuille, M., R. S. Bradley, and F. Keimig, 2000: Climate variability in the Andes of Ecuador and its relation to tropical Pacific and Atlantic sea surface temperature anomalies. *J. Climate*, **13**, 2520–2535, doi:10.1175/1520-0442(2000)013<2520:CVITAO>2.0.CO;2.

Wagemann, J., B. Thies, R. Rollenbeck, T. Peters, and J. Bendix, 2015: Regionalization of wind-speed data to analyse tree-line wind conditions in the eastern Andes of southern Ecuador. *Erdkunde*, **69**, 3–19, doi:10.3112/erdkunde.2015.01.01.

Wilson, J. W., and E. A. Brandes, 1979: Radar measurement of rainfall—A summary. *Bull. Amer. Meteor. Soc.*, **60**, 1048–1058, doi:10.1175/1520-0477(1979)060<1048:RMORS>2.0.CO;2.

Wood, R., 2005: Drizzle in stratiform boundary layer clouds. Part II: Microphysical aspects. *J. Atmos. Sci.*, **62**, 3034–3050, doi:10.1175/JAS3530.1.

Wulfmeyer, V., and Coauthors, 2008: Research campaign: The Convective and Orographically Induced Precipitation Study. *Bull. Amer. Meteor. Soc.*, **89**, 1477–1486, doi:10.1175/2008BAMS2367.1.

——, and Coauthors, 2011: The Convective and Orographically-induced Precipitation Study (COPS): The scientific strategy, the field phase, and research highlights. *Quart. J. Roy. Meteor. Soc.*, **137**, 3–30, doi:10.1002/qj.752.

Xie, H., X. Zhang, B. Yu, and H. Sharif, 2011: Performance evaluation of interpolation methods for incorporating rain gauge measurements into NEXRAD precipitation data: A case study in the Upper Guadalupe River basin. *Hydrol. Processes*, **25**, 3711–3720, doi:10.1002/hyp.8096.

Zollo, A. L., V. Rillo, E. Bucchignani, M. Montesarchio, and P. Mercogliano, 2016: Extreme temperature and precipitation events over Italy: Assessment of high-resolution simulations with COSMO-CLM and future scenarios. *Int. J. Climatol.*, **36**, 987–1004, doi:10.1002/joc.4401.